

₁ Preliminary design studies of a drift tube detector for
₂ SHiP experiment

₃ Bereziuk Ivan
₄ July 12, 2015

5 1 Introduction

6 ¹ The completion of the particle content of the Standard Model (SM) with the discovery of the
7 Higgs boson, and advances in cosmology highlight the necessity for a new level of understanding
8 of physics Beyond the Standard Model (BSM) . At the same time, neither experiment nor theory
9 provide clear hints of the nature or the scale of this new physics.

10 Over the next decades the Fermi-mass scale, and even beyond, will be comprehensively
11 explored either directly by ATLAS and CMS at the LHC, or indirectly, assuming generic
12 couplings, at experiments like LHCb, Belle2 and NA62 [4]. Hidden particles, which interact very
13 weakly with the SM particles, are predicted in many theoretical models capable of explaining the
14 shortcomings of the SM. A large part of their accessible parameter space remains unexplored.

15 In this situation SHiP is a recently proposed new general purpose fixed target facility at
16 the SPS which is aimed at exploring the domain of hidden particles and make measurements
17 with tau neutrinos. Hidden particles are predicted by a large number of models beyond the
18 Standard Model. The high intensity of the SPS 400 GeV beam allows probing a wide variety
19 of models containing light long-lived exotic particles with masses below $10 \text{ GeV}/c^2$, including
20 very weakly interacting low-energy SUSY states.

21 1.1 Overview of the Experiment

22 At the energy accessible at the SPS, the hidden particles are predominantly produced in decays
23 of hadrons, in particular in decays of charmed and beauty hadrons above the kaon mass, and
24 in proton bremsstrahlung.

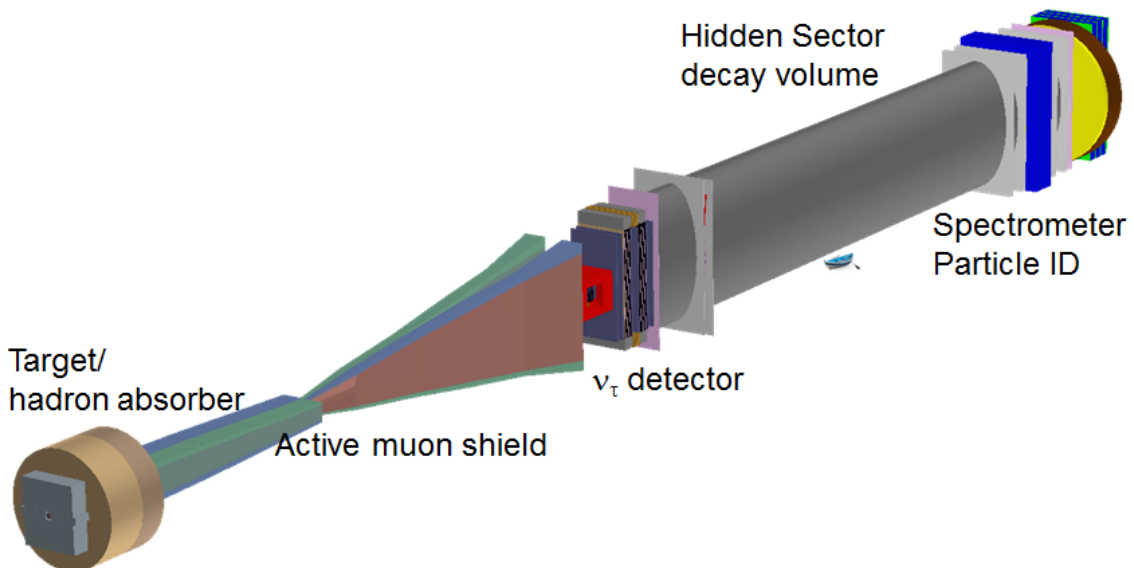


Figure 1: Overview of the SHiP facility [3]

¹This section mostly(The information of for this section was) taken from SHiP Technical Proposal (TP) document [3] just to overview the experiment and prepare reader for subsequent work under separate part of detector.

25 The detector for the direct detection of the hidden particles is designed to fully reconstruct
 26 their exclusive decays. Table 1 summarizes the main decay modes of the hidden particles in
 27 the various models considered.

Table 1: Summary of the main decay modes of hidden particles in various models ($\ell = e, \mu$).

Models	Final states
Neutrino portal, SUSY neutralino	$\ell^\pm\pi^\mp, \ell^\pm K^\mp, \ell^\pm\rho^\mp, \rho^\pm \rightarrow \pi^\pm\pi^0$
Vector, scalar, axion portals, SUSY sgoldstino	$\ell^+\ell^-$
Vector, scalar, axion portals, SUSY sgoldstino	$\pi^+\pi^-, K^+K^-$
Neutrino portal ,SUSY neutralino, axino	$\ell^+\ell^-\nu$
Axion portal, SUSY sgoldstino	$\gamma\gamma$
SUSY sgoldstino	$\pi^0\pi^0$

28 The principal background to the hidden particle decay signal originates from the inelastic
 29 scattering of neutrinos and muons in the vicinity of the detector producing long-lived particles.

30 The beam line is designed to minimize the background sources. The proton interaction in
 31 the target gives rise to a copious direct production of short-lived resonances, and pions and
 32 kaons. While a hadron stopper of a few metres of iron is sufficient to absorb the hadrons and
 33 the electromagnetic radiation emerging from the target, the decays of pions, kaons and short-
 34 lived resonances result in a large flux of muons and neutrinos. In order to reduce the flux of
 35 neutrinos, in particular the flux of muon neutrinos and the associated muons, the pions and
 36 kaons should be stopped as efficiently as possible before they decay. The target must therefore
 37 be made of a material with the shortest possible interaction length and be sufficiently long to
 38 contain the hadronic showers with minimum leakage. Since the production angle of the hidden
 39 particles is relatively large, there is no requirement to minimize the beam spot.

40 The short-lived resonances and the residual flux of decaying pions and kaons still give rise to
 41 a large flux of muons. This flux must be efficiently cleared from the detector fiducial volume by
 42 either a passive shield or through an active shield based on magnetic deflection. The residual
 43 flux should also be low enough so not to compromise the occupancy limit in the tau neutrino
 44 detector. As illustrated in Figure 1, in the baseline design a 5 m horizontally wide region
 45 respecting these requirements has been achieved with a 48 m long active muon shield based on
 46 magnetic deflection of the muons in the horizontal plane.

47 The muon shield is followed by the 10 m long tau neutrino detector, which puts the start of
 48 the HS decay volume at about 64 m [3]. The main purpose of the tau neutrino detector is to
 49 perform the first direct observation of the $\bar{\nu}_\tau$, and to study the properties and the cross section
 50 of ν^τ and $\bar{\nu}_\tau$. The current optimization of muon shield and cost, results in a decay volume with
 51 an elliptical shape of 5 m width and 10 m height. The length of the decay volume is obtained
 52 by maximizing the acceptance to the hidden particle decay products given the transversal size.

53 The full reconstruction of the hidden particle decays requires a magnetic spectrometer and
 54 a system for particle identification at the end of the decay volume.

55 The particle identification system requires an electromagnetic calorimeter for e/γ identifica-
 56 tion with sufficient granularity and energy resolution in order to reconstruct π^0 's, and a hadron
 57 calorimeter in combination with a muon detector for π/μ separation.

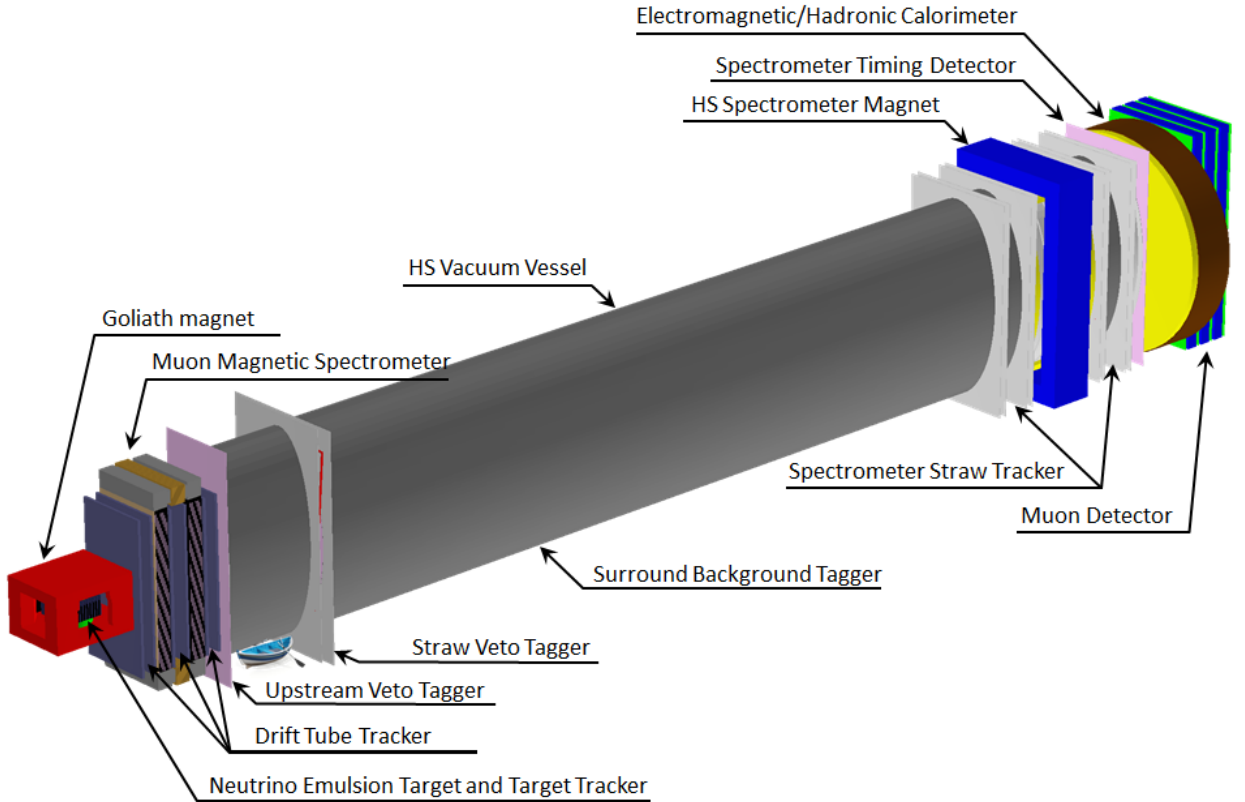


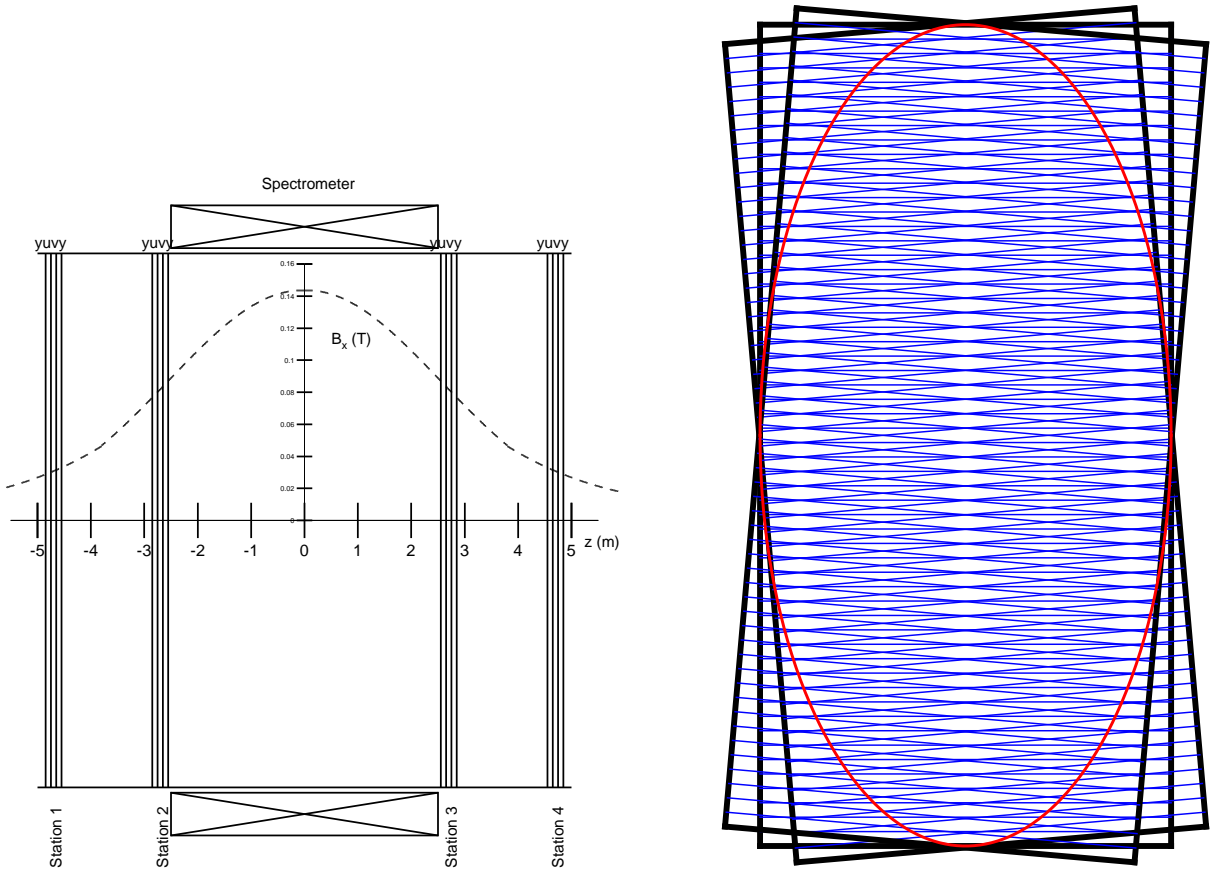
Figure 2: SHiP detector layout

58 1.2 Spectrometer tracker

59 Spectrometer tracker is a part of particle identification system. The purpose of the HS spec-
 60 trometer is to reconstruct with high efficiency the tracks of charged particles from the decay
 61 of hidden particles. The spectrometer must provide an accurate determination of the track
 62 momentum and of the flight direction within the fiducial decay volume.

63 The spectrometer consists of a large aperture dipole magnet and two tracking telescopes on
 64 each side of the magnet. A layout with four tracking stations symmetrically arranged around
 65 the dipole magnet, as depicted in Figure 3a, is taken as a baseline. The size and layout of the
 66 tracker stations is connected to the size of the magnet. A dipole spectrometer magnet with a
 67 horizontal gap of 5 m, a height of 10 m and a length of 5 m provides good acceptance coverage
 68 and is considered feasible at a reasonable cost.

69 Following the direction of the magnetic field, the measuring elements are oriented horizon-
 70 tally to measure precisely the vertical (Y) coordinate. Two stereo views (U and V) are rotated
 71 by an angle $\pm\theta_{stereo}$ for measuring the transverse coordinate X with an accuracy degraded by
 72 $\sim 1/\sin\theta_{stereo}$. The precision in X (i.e. the value of the stereo angle) is driven by the need
 73 of a good enough measurement of the decay vertex, opening angle of the daughter particles
 74 (which enters the invariant mass) and impact parameter at the production target. Each station
 75 contains 4 views (Y-U-V-Y). The two stations on the same side of the magnet are separated by
 76 $\Delta = 2m$ and a gap of 5m is left between the second and third stations (i.e. each is 2.5m away
 77 from the centre of the magnet).



(a) Position of the tracking stations and dipole magnet, overlaid with magnetic field component B_x as a function of z .

(b) Four views in one station (not all straws shown, for the sake of clarity). The nominal acceptance, defined by the vacuum vessel, is shown as a red ellipse.

Figure 3: Spectrometer layout

The tracking stations of the magnetic spectrometer must provide good spatial resolution and minimise the contribution from multiple scattering. In addition, the tracker must operate in vacuum. A straw tracker made of thin polyethylene terephthalate (PET) tubes is ideal to meet these goals. Gas tightness of these tubes has been demonstrated in long term tests and the mass production procedure is also well established (see NA62 experiment [4]). The main differences between the SHiP tracker and the NA62 tracker are the need for 5 m long straws (vs 2.1 m in NA62). The main changes with respect to the Expression of Interest [6] follow from the changes applied to the spectrometer magnet. The straw orientation has been turned from vertical to horizontal and one transverse dimension has been increased from 5 to 10 m.

2 Subject of study

With new requirements for new straw tracker we have important challenge for long straws. It is related to the fact of straw and wire will be subjected by gravitational and electrical forces and cause sagging. Because the straws are oriented horizontally (or almost, in case of stereo

91 views), sagging is expected to cause in most drift tubes a downward deflection, which might be
92 exploited when applying a correction.

93 Undoubtedly the presence of sagging may complicate the data processing stage and some-
94 what worse accuracy of track reconstruction. Primary question we have to investigate "is
95 acceptable sag-admitting design?" and "What a downgrade of precision for sag-admitting de-
96 sign?".

97 Results of measurements on prototypes are discussed in Section 8.

98 3 Signal

99 Computer program Garfield [1] is designed for detailed simulation of two- and three-dimensional
100 drift chambers. So we will perform STRAW tube studies using this program.

101 Charged particle create electron-ion pairs while traverse the drift tube. Electrons under
102 affecting the electric field drift to the wire anode (see figure 4). During the travel they increase
103 their energy and invoke an avalanche. Therefore they produce a measurable signal.

104 Initial electrons drift to the wire due to the electrical field between the wire and the tube
105 wall. Electrons ionize gas molecules due to the high electric field around the wire, especially
106 near the wire when the electric becomes very strong. Subsequently readout electronics process
107 the signal induced on the wire.

108 The event registers if signal reach some a threshold voltage (Fig. 5). So the value of threshold
109 is a key factor on the way of searching optimal setting for signal processing procedure.

Table 2: STRAW tube parameters

Parameter name	Value
wire	$30\mu m$ gold-plated Tungsten
straw length	5m
Voltage	1750V
inner tube radius	9.8 mm
wire medium density	$19.3 g/cm^3$
Wire tension	$\sim 90 g$
Working tube gas mixture	Ar70% CO ₂ 30%

110 We have to set threshold as low as possible but enough above from noise level to achieve
111 best rate of true/false detected tracks and highest track registration precision and efficiency.

112 A variation of the signal height introduces a variation in the time when the signal passes
113 the threshold and is considered to be the main contribution to the STRAW tracker resolution.

114 In the track reconstruction software(GARFIELD [1]) an effective TR-relation is used. It only
115 describes the relation between the drift time and the distance from the track to the wire, which
116 differs from the distance to the ionization cluster. The shape of the TR-relation is defined by
117 the drift velocity of the ionization cluster inside the straw. The electric field increases towards
118 the wire, leading to a non linear TR-relation.

119 The drift time versus the unbiased distance distribution and the result of the fit are shown
120 in Fig. 17a. Noise hits under the main distribution, i.e. at earlier times, are due to primary
121 or secondary particles (δ -rays) passing the straw at a closer distance to the wire, consequently

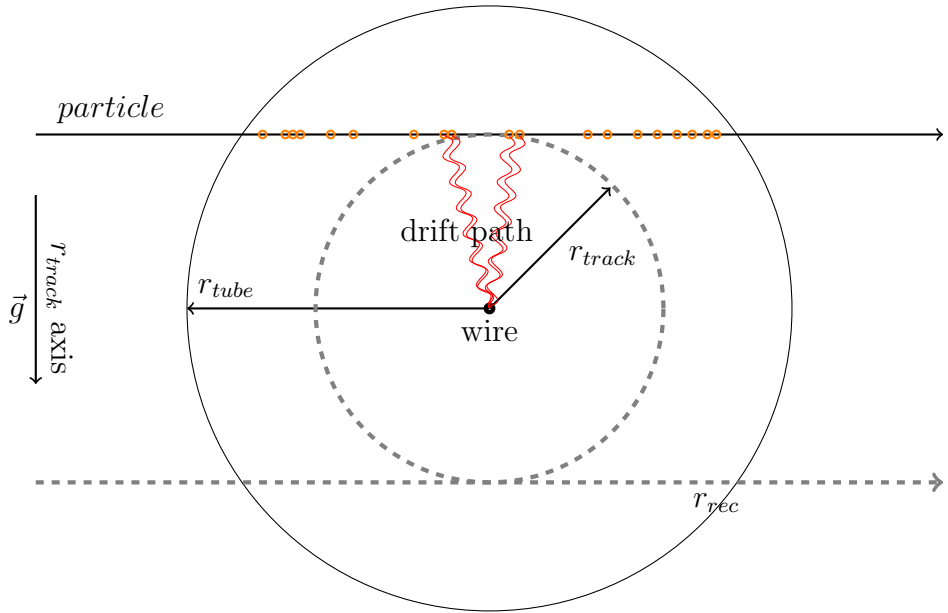


Figure 4: Schematic view of a particle passing the straw and producing ionization clusters(orange points). The ionization cluster electrons drift to the wire and induce the signal. The closest distance from the track to the wire, r_{track} , and radius of the straw, $r_{tube} = 2.45\text{mm}$, are also indicated.

¹²² producing an earlier signal. Initial clusters along the track are marked by orange points on the
¹²³ figure.

¹²⁴ Muon μ was chosen as test particle for simulation with energy 1GeV . You can see some of
¹²⁵ typical tracks from the μ through the tube Fig.10a,10b.

¹²⁶ 3.1 Leakage noise

¹²⁷ Every time we deal with different kind of noise. Basically it is noise from leakage current
¹²⁸ through readout electronics.

¹²⁹ As will be discussed further we analyse not the current invoked by particle but the output
¹³⁰ voltage from amplifier. In GARFIELD we able convolute input current $I(t)$ with electronic
¹³¹ response function (1)²

$$f_{resp} = A \cdot (e^{-t/0.005} - e^{-t/0.030}) \quad (1)$$

¹³² Noise is very important for every calculations and it makes bit impact on straw precision
¹³³ and straw efficiency. So we can't rely on results until we receive signal and noise from real
¹³⁴ STRAW tube prototypes.

¹³⁵ Convolution of input current make it smooth. Usually in typical conditions³ noise have
¹³⁶ gauss distribution with RMS equal to a amplitude of signal from 2000 electron in the tube -

²in this equation t in nanoseconds

³as in table 2

¹³⁷ electric noise charge (ENC)⁴ In fig.5 you can see deposition from noise marked by blue line.
¹³⁸ On the Fig.5 The timestamp $Time = 0$ correspond to the time muon hits a tube. The
¹³⁹ convolution function smooths and spreads input current. It mean that the output voltage in
¹⁴⁰ GARFIELD does not contain part of signal before hit event timestamp.

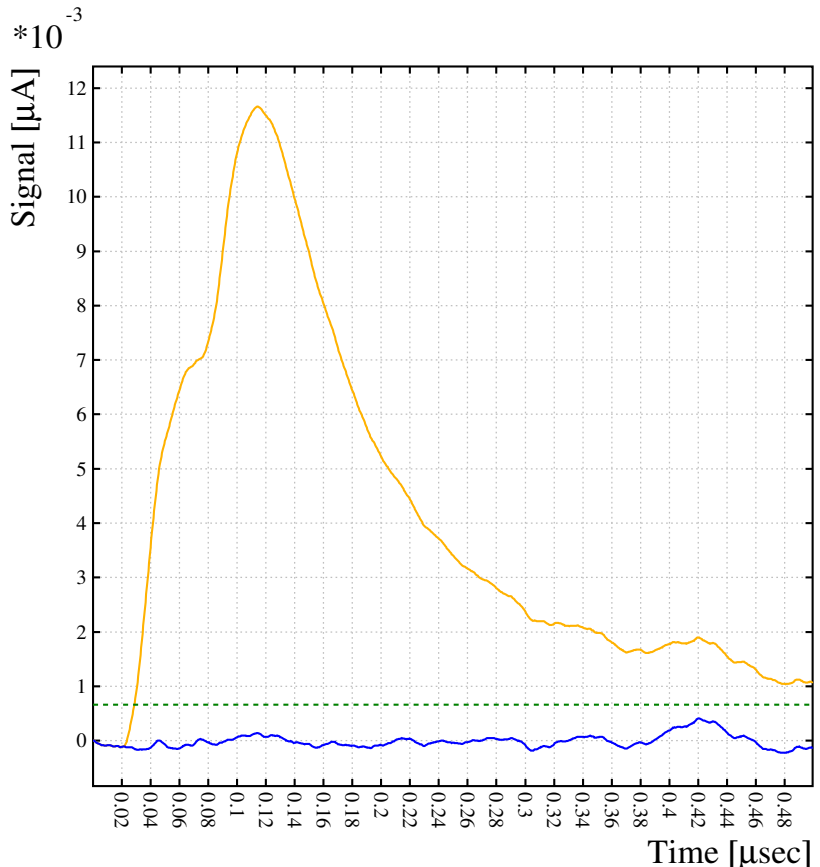


Figure 5: Example of output signal $V(t)$ after convolution(front-end electronics) from central track(yellow line). The noise component of the same signal depicted by separate blue line. Grin dashed line is a threshold for trigering drift time and equal to 5σ of noise distribution.

¹⁴¹ 3.2 STRAW efficiency

¹⁴² The interaction of charge particle with gas molecules have probabilistic nature. For short
¹⁴³ distance tracks(somewhere near the tube wall) the probability of tracks that do produce zero
¹⁴⁴ electron/ion pair becomes significantly high.

¹⁴⁵ The number of produced ionization clusters directly affects the hit efficiency profile. [2]
¹⁴⁶ Smaller ionization length increase hit efficiency because of more ionization clusters per length
¹⁴⁷ unit are producing. In GARFIELD we can easily calculate amount of clusters per track. In fig.

⁴With testing of real 5 m long straws and ultimate examples of electronics we will measure real noise. But for now is only close to reality suggestion concerning whis.

¹⁴⁸ 7b you can see a distribution of number of clusters per central track for our STRAW tube. It
¹⁴⁹ mean that straw efficiency will be lower near the tube wall(see Fig.6).

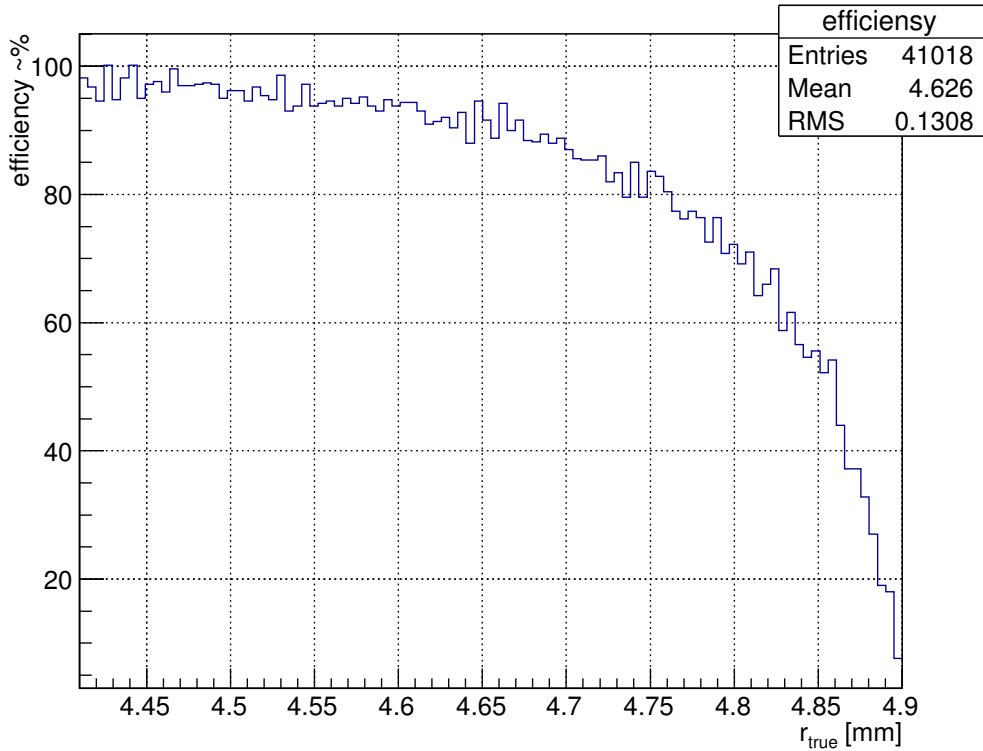


Figure 6: Straw tube efficiency. Result of homogeneous penetrating periphery of tube by 50k events(scaled down by factor of 5. $\frac{50k \text{ events}}{100\text{bin}} = 500 \frac{\text{events}}{\text{bin}}$).

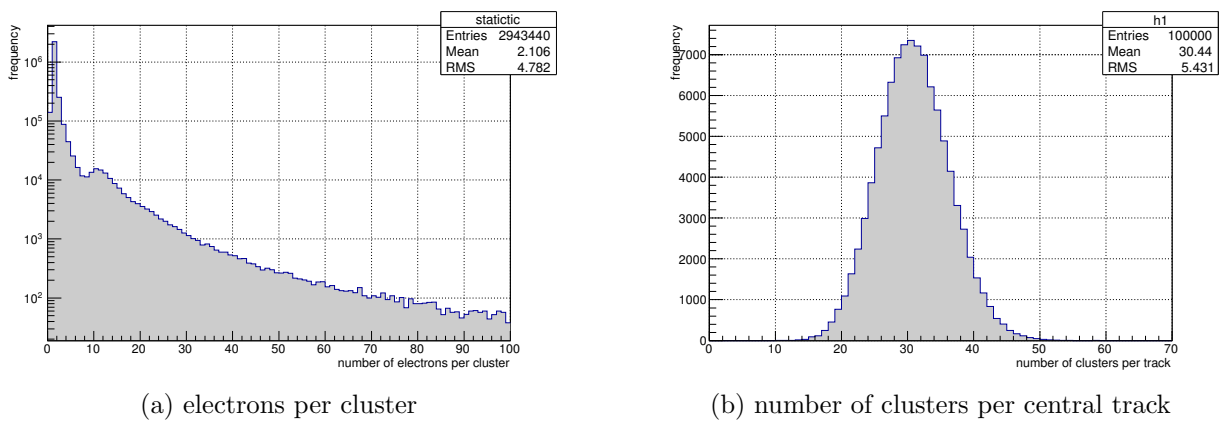


Figure 7: Statistics info from GARFIELD about track from $1GeV \mu$. Tube described in table 2

¹⁵⁰ From the Fig.6 we can conclude that the efficiency of tube is 100% almost in whole region

151 covered by tube except pre wall region which is quite small. Increasing the gas mixture density
152 or increasing the tube radius for the same gas density can increase tube efficiency.

153 4 Gain

154 Lets look on avalanche process in the tube. If multiplication occurs, the increasing of the
155 number of electrons per path ds is given by

$$dN = N\alpha ds \quad (2)$$

156 The coefficient α is determined by the excitation and ionization cross sections of the elec-
157 trons that have acquired sufficient energy in the field. It also depends on the various transfer
158 mechanism and electric field E and increases with the field because the ionization cross-section
159 goes up from threshold as the collision energy ε increases. As we can suppose the coefficient α
160 is of big amount of parameters.

161 The amplification factor G on a wire(that is more interesting for us) is given by integrating
162 (2) between the point s_{min} where the field is just sufficient to start the avalanche and the wire
163 radius a :

$$G = N/N_0 = \exp \int_{s_{min}}^a \alpha(s) ds \quad (3)$$

164 GARFIELD can provide us by amplification factor G for any point of the tube(because G
165 is coordinate dependent magnitude). The amplification factor is equal almost in whole tube
166 space except neighbourhood near the wire because electric field becomes significantly high only
167 near the wire (see figs 8a, 8b). When the wire is shifted from the center of the cube the electric
168 field in area close to the wire is the same as in centered state. So the amplification factor G is
169 quite similar in both cases.

170 Implementation of gain value calculation is not so reliable in GARFIELD(especially for-
171 tran version). Gain should be recalculated using Garfield++ (which is newer and take into
172 consideration more effects).

173 On the Fig. 9 you can see that the gain $G(V)$ have precisely exponential dependence. This
174 is frankly does not inspire confidence. The difference can be up to 100% (as Rob Veenhof -
175 creator of GARFIELD [1] said).

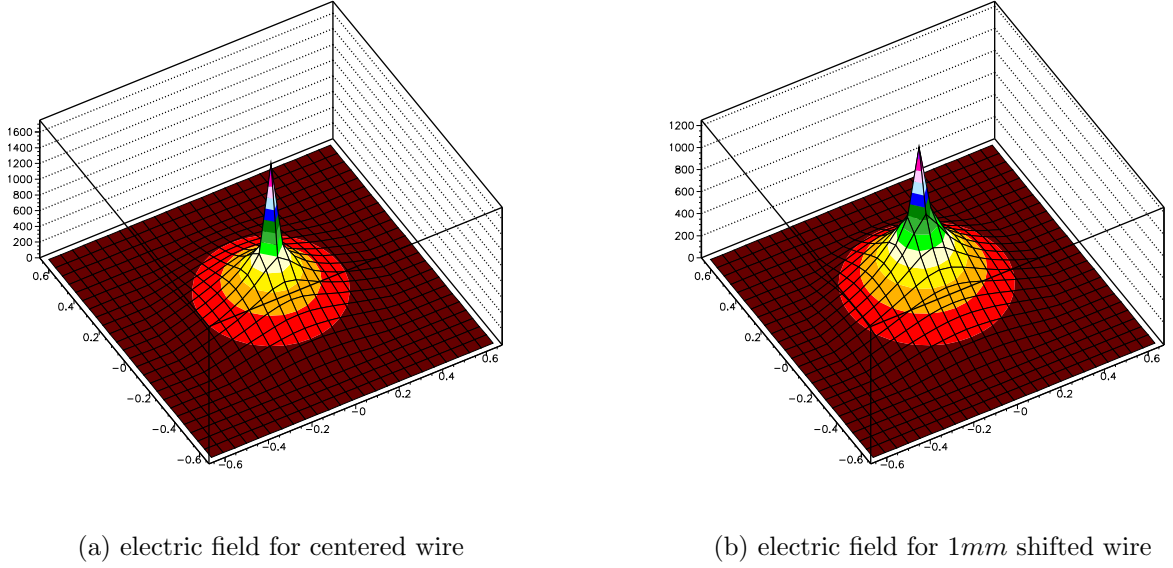


Figure 8: Electric field intensity map for different wire position in the cube calculated in GARFIELD software. Conditions for those plots are described in table 2

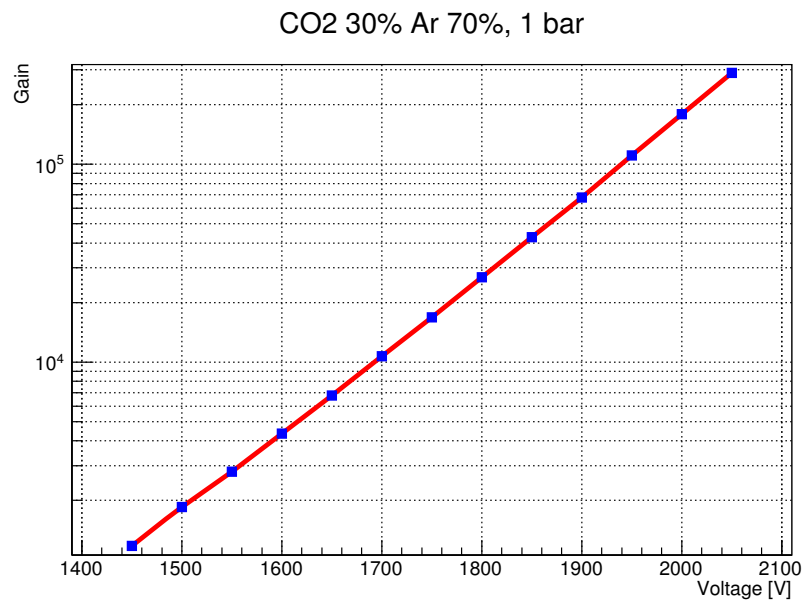


Figure 9: Dependence of the gain of the voltage applied to the wire. The rest of STRAW tube settings correspond to table 2.

176 5 Wire sagging

177 Easy to predict that the displacement of the wire invokes distorting an electric field(see
 178 figs 8a,8b) and drift path for electrons/ions inside the tube(see fig.10a and fig.10b). The rt-
 179 relation for track reconstruction directly depend on the wire position in the tube. So rt-relation
 180 lose it's previous symmetry(see next sections).

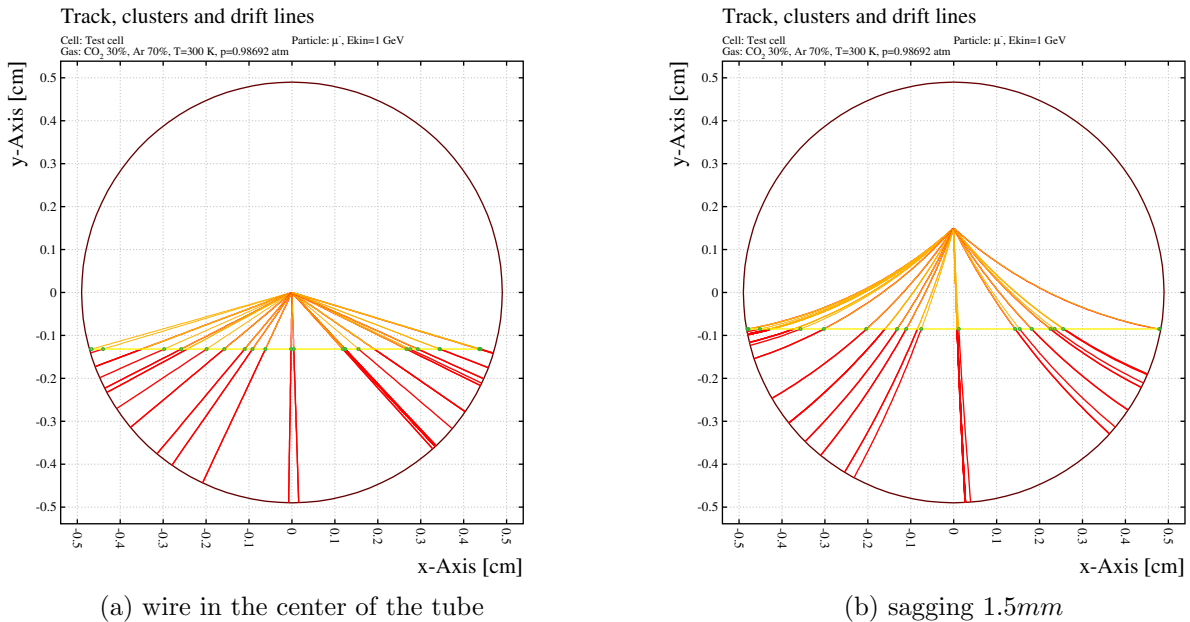


Figure 10: An example of tracks from the on the tube for different position of the wire from GARFIELD simulations. Initial clusters marker by green. Drift lines for electrons marked by yellow, ions – red lines.

181 The direction of sagging is unpredictable when the wire is centered and the straw has vertical
 182 orientation. Impact of gravitation field into the wire does not make any effect in this state.
 183 But we can avoid this ambiguity by setting straws horizontally. This condition is necessary
 184 to make track reconstruction possible. Even when strung with a pulling force T close to the
 185 breaking limit, wires in several metre long tubes will experience a gravitational sag that is large
 186 in comparison with the achievable accuracy of drift tubes.

187 We estimate significant wire sagging(by comparison to the tube radius) because of wire
 188 attracts to the tube under affecting of gravitation and electric field force.

189 You can see a profile of wire sagging of 5m length wire in 1cm diameter straw tube and
 190 1750V voltage on the fig.11 calculated in GARFIELD software [1].

191 The calibration of STRAW tube with sagged wire is more difficult by comparison to the
 192 mode without sagging.

193 Variation of wire tension, wire radius should be taken into account as high affect factor for
 194 sag value.

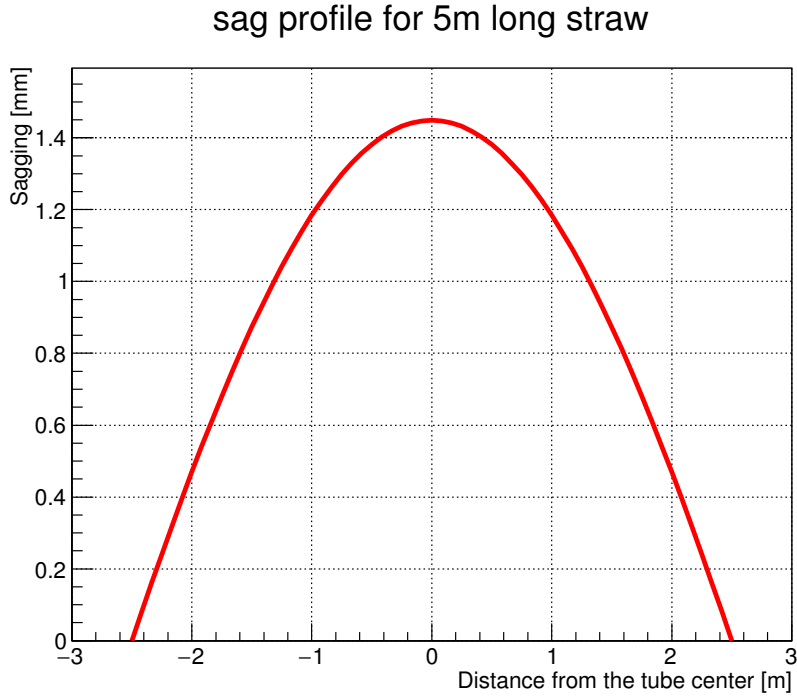


Figure 11: Wire sag profile under electric and gravitation field calculated in GARFIELD. All options for this straw system are described in table 2.

195 6 Sag estimation

196 In this section we have to find out method for assessing sagging. This is key step that makes
 197 track reconstruction procedure possible.

198 At first we have to think on data we can use for such kind of calculations. Much attractable
 199 information we can extract from drift time distribution.

200 The wire sags under electric and gravitation force. Therefore the sag value is differ along the
 201 tube(fig 11). But we can separate collected data for different position along the tube. STRAW
 202 tube detector consist of several parallel layers of tubes at some angle to each other. So we can
 203 easily fix longitudinal position(along the tube) for tracks that cross several crossed tubes(at
 204 least two). Collimation is also possible via scintillator triggering before and after STRAW
 205 tube.

206 Lets say we can install our STRAW tube into homogeneous particle flow and save drift time
 207 distribution for some narrow section of the tube. These distributions are different from each
 208 other(see example on Fig.12). The difference between diagrams increasing with sag difference.
 209 So it is good tools for sag calibration.

210 Then we have to bind each drift time distribution with appropriate sag value. This is part
 211 of laboratory work when sag profile measurements can be performed via optical method prior
 212 to the exposition.

213 Distributions on graph 12 contain GARFIELD simulations for some certain wire(not for
 214 section of sagged wire)because of GARFIELD can handle only two-dimensional tasks.

215 Lets say we have an equipment for scanning the tube to measure wire sagging profile. After

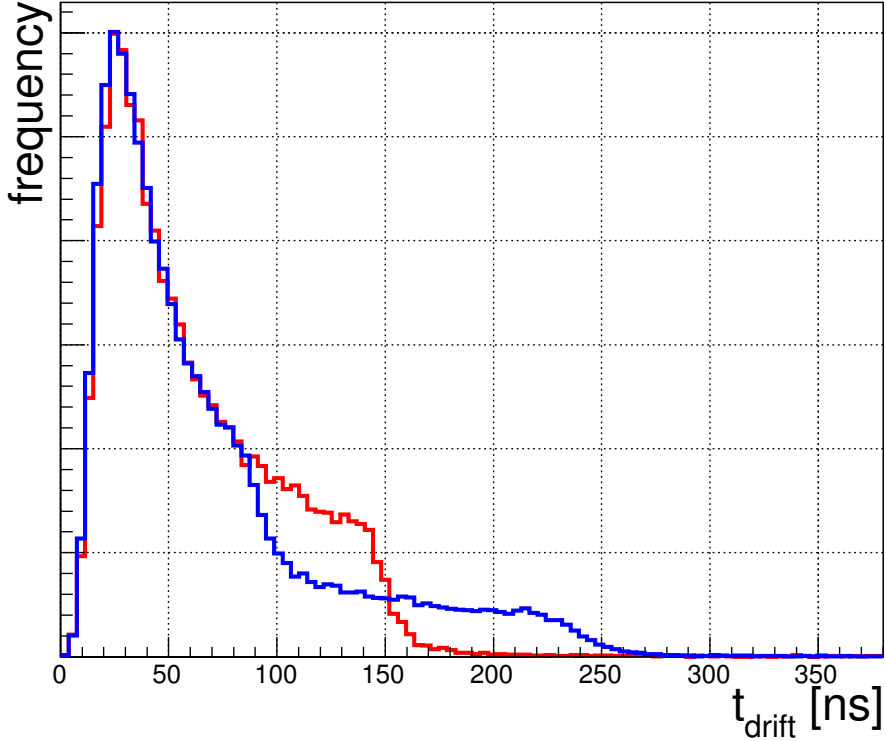


Figure 12: Drift time distribution for a homogeneous irradiation with a centered wire (red) and for a wire offset of 0.9 mm (blue).

profile measurements we divide our tube into sections. Wire position within separate section should be within desired precision.

So we need divide our tube into 57 sections (see figure 13) if maximum of wire offset(at the center of the tube) is equal to 1.45mm and desired precision is $50\mu\text{m}$.

$$N_{halftube} = \frac{1.45\text{mm}}{50\mu\text{m}} = 29; \quad (4)$$

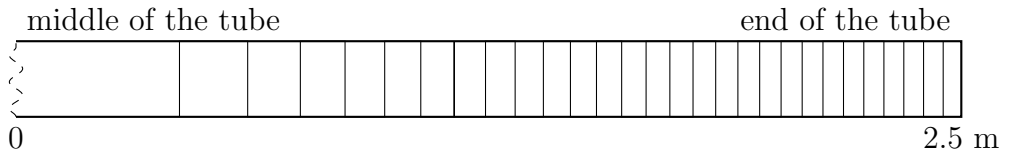


Figure 13: Tube sectioning. Sag value at the tube center is 1.45mm . Difference of wire sag value from section to section is $50\mu\text{m}$

Then we need an exposition of sufficient number of events for every of sections(at least 50k events). There can be troubles time of exposition time because square of sections at the end of the tube is quite small. So the time of exposition of distant sections will be inversely much longer.

224 The next step is to find dependence of dt-distribution shape with wire offset. The point that
225 we can evaluate matching between histograms via χ^2 criteria. As we can see in the figure 14a
226 the comparison of χ^2 has smooth dependence across increasing of wire offset for high statistic
227 histograms.

228 First steps for sag estimation are:

- 229 1. measure wire sag profile via optical method;
- 230 2. make a sectioning of tube due to wire sag profile;
- 231 3. collect enough amount of events for every of dt-distribution and save this *core* distribution
232 for further comparisons.
- 233 4. measure dt-distribution of tube section that is subject of study and adjacent area.
- 234 5. calculate χ^2 criteria for this current dt-distribution with each of core distribution.
- 235 6. correlate found values of wire displacement relatively to the adjacent sections or by fitting
236 of whole wire profile points.

237 **6.1 Finding most probable value of wire displacement for certain 238 point of the tube**

239 **6.2 Raw method**

240 The simplest method to find S is to equate it to the corresponding value of best matched core
241 DT-histogram.

242 On the figure 14b you can see distribution of such kind of reconstruction. Even for 5k events
243 td-distribution in this case the precision can be quite high($\sim 50\mu m$). This method limited by
244 core DT-diagram stepping.

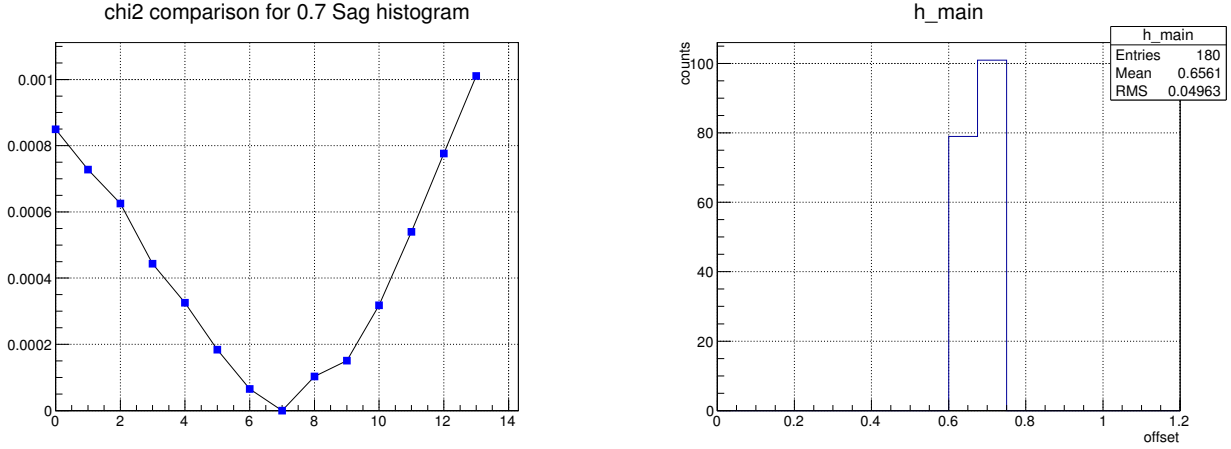
245 **”Minimum of χ^2 as linear approximation”**

246 If dependence of χ^2 criteria of wire displacement S for near to the true position region is
247 linear(that certainly is not a true, but as first approximation) than we can easily find this
248 intermediate value of wire displacement.

249 There we proceed in two steps. The first is raw estimation of wire displacement as in above
250 mentioned method.

251 For the second step we need to know some additional estimations. The first question is
252 how small can be χ^2 in our case? Lets fix statistic on 50k events for one DT-distribution. This
253 value should a bit depend for different S . But for now lets consider that it is a constant value.
254 From the Fig.15a you can see distribution of χ^2 from comparison of 20 DT-distribution⁵ for
255 $S = 0.7mm$. Mean value + RMS of distribution is $5.3 * 10^{-5}$. So if some of the χ^2 is higher
256 than this threshold than we go for second stage.

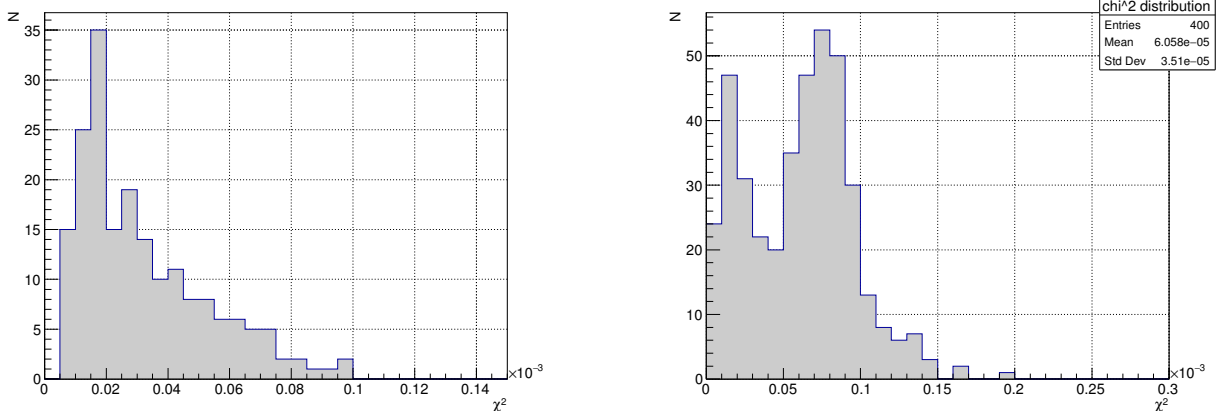
⁵pair comparison give us $C_{20}^2 = \frac{20!}{2!18!} = 190$ different combinations



(a) Series of χ^2 of comparison 0.7mm sag core td-distribution with each each of core histograms. 14 core histograms for sag diapason 0...1.3mm with step of $100\mu\text{m}$

(b) Distribution of wire offset reconstruction from 180 series 5k events each. 50k events for core template histograms. True bias is 0.63mm. 1 bin = 0.1 mm.

Figure 14: Wire position(displacement) reconstruction



(a) χ^2 distribution of comparison of 20 DT-distributions diagrams each other ($C_{20}^2 = 190$ combinations)

(b) χ^2 distribution of comparison DT-distribution histograms 0.6mm S vs 0.7mm

Figure 15: Comparison of χ^2 distributions for self-comparison of DT-distribution diagram.

On the Fig.14b you can see distribution of wire sag calculation for 180 histograms with 5k events statistic. Precision in this case $\sim 50\mu\text{m}$. The algorithm of sag estimation is pretty simple: wire offset value is equal to the offset of best matched core histogram.

After we know sag value at some points of the tube or every where we can make one awesome collective analysis. The smoothing of wire offset value along the tube will give to us much more precision results.

From the Fig.15b the distribution of χ^2 for adjacent point have narrower distribution by comparison to "self-comparison" χ^2 distribution. Therefore calculation of S from analyse of consecutive smallest χ^2 values can improve precision. Need to say that collective approach to

266 this task also can improve precision of S finding.

267 6.4 Practical measurements of DT-distribution

268 We need second detector that can measure position of muon that hit STRAW tube. It can be
269 Si strip sensor based detector or detector based on scintillation with the same destination.

270 Each kind of detector have it's own advantages and disadvantages. The potential cell unit
271 (strip or pixel) of Si detector will be smaller than in scintillator but also is much expensive. At
272 the current stage we deal with 1cm diameter tubes. So scintillator is primal target. But it can
273 shift to the Si sensors if scintillators will not provide satisfied precision.

274 Preliminary chem of DT-measurements you can see on the picture Fig.16

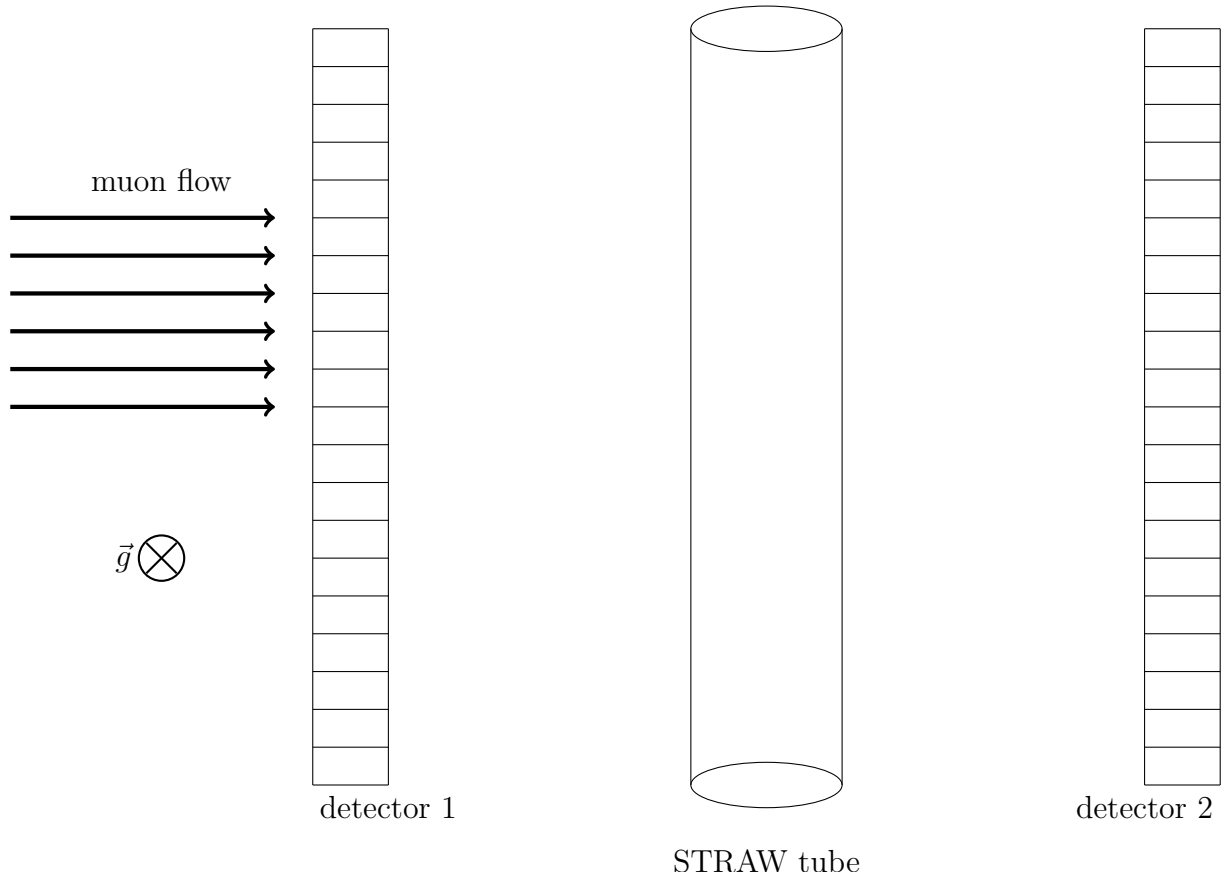


Figure 16: principal layout of measurement of core DT-distribution histogram

275 In this method detector before tube (D1) and detector placed after the tube(D2) in total
276 should provide sufficient precision for track reconstruction to be able distinguish tracks for
277 different section of the tube (approximately as shown on the Fig. 13). Muon flow should be
278 homogeneous and so D1 and D2 also should cover full acceptance of the tube.

279 The profile of the wire sagging can be measured by optical method. Walls of the tube is
280 very thin, so it can be simplest way to get sag profile.

281 7 Track reconstruction

282 The time between the track hit time stamp and the signal rising edge is a measure of *drift time*
 283 of these electrons. The relation between the *drift time* and the distance from the track to the
 284 center of the tube(wire while no sag for centered wire) is called *drift time - distance* relation or
 285 *tr-relation*.

286 The drift time t is a function of track position (relative to the wire) and electric field along
 287 the drift trajectory.

288 Assumed that the working position for straws will be parallel to the particle bunch, and
 289 acceptance of particle spreading will not be significantly big. So tracks will be collinear each
 290 other within every separate STRAW tube unit.

291 Summing the above mentioned we have one dimension task – reconstruct tracks on vertical
 292 axis⁶ (see examples of outcome tr-distribution $t = t(r, s = 0)$ in Fig.17a and Fig.17b) even the
 293 wire sagging. Sagging will be always down thanks to gravitation force \vec{g} .

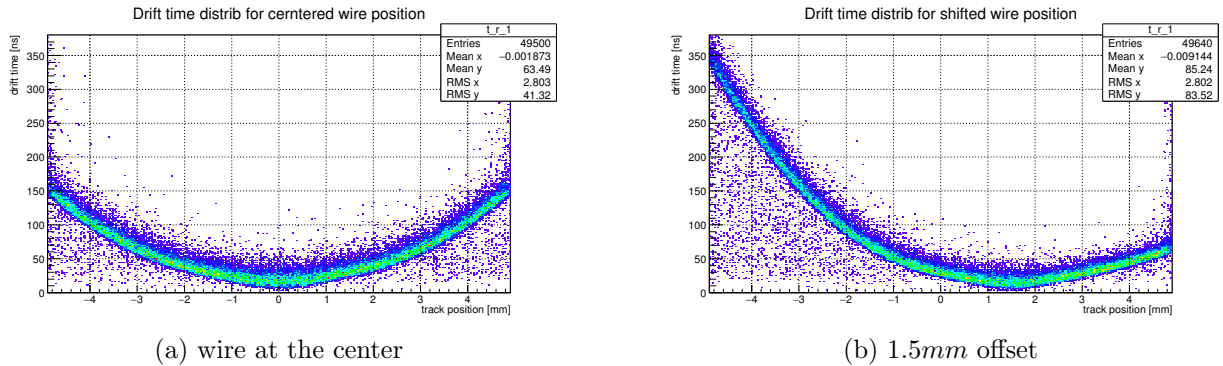


Figure 17: Distribution of drift time t_{drift} as function of track position r_{track} relatively to the tube center

294 The rt-relation is differ along the tube because different wire position s . Thus we have for
 295 the drift time

$$t_{drift} = t_{drift}(r_{track}, s) \quad (5)$$

296 The idea to STRAW tube is to find the inverse dependence

$$r_{track} = r_{track}(t_{drift}, s) \quad (6)$$

297 From the section "Sag estimation" we can find sag profile for straw. Therefore the rt-
 298 calibration becomes 1 dimension less:

$$r = r(t, s = const) \quad (7)$$

299 7.1 How drift time resolution depend on wire offset?

300 Distorting of electric field inside the tube invoked by wire displacement from the center position
 301 will make an effect on drift time. Here we are going to estimate magnitude of drift time change.

⁶An example of single track reconstruction which explains the approximate procedure of reconstruction you can see on Fig.4

302 As was noted above we make a binning for our data along the r_{track} (fig. 17a, 17b). The
 303 resolution at every bin is RMS of every bit digram (fig.??).

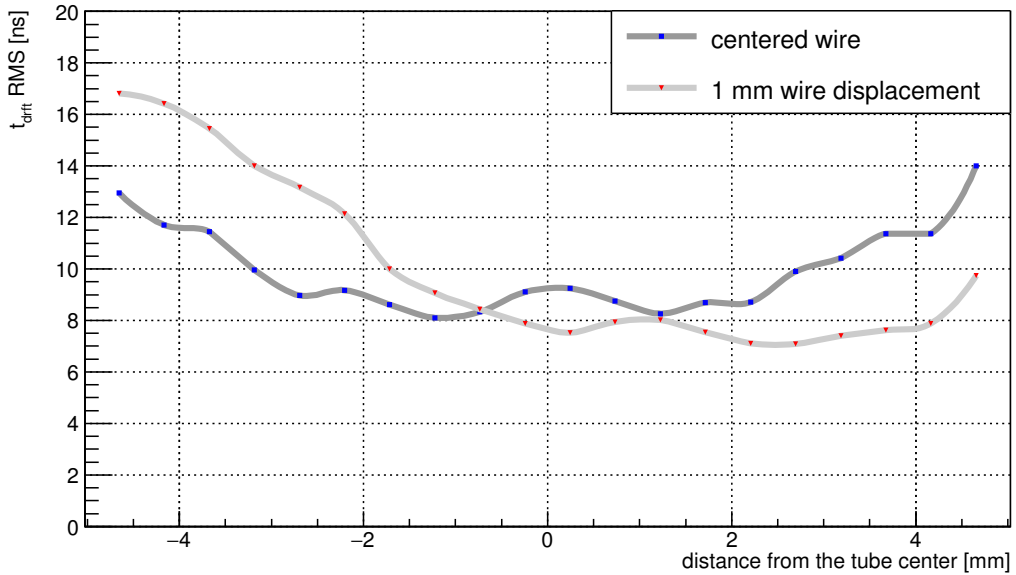


Figure 18: Resolution of drift time as a function of distance from the wire.

304 We are dealing with probabilistic nature of clustering that spread rt-relation from thin line.
 305 The leakage noise is also present in calculation but the effect of it is not very high(especially
 306 in this calculation).

307 Every plot of output current (see fig. 5) consist of 1000 equidistant frames. The threshold
 308 is set to 5σ of noise. Leakage noise make effect on drift time measurements in case its amplitude
 309 becomes higher than threshold value in range from $t = 0$ to $t = t_{drift}$. At five-sigma there is
 310 only one chance in nearly two million that a random fluctuation would yield the result. The
 311 drift time for tracks close to the tube edge can be up to 150ns and 300ns in case wire displaced.
 312 The probability to meet noise above threshold value is less than 0.02%.

313 Another source of noise points on tr-distribution comes from δ -electrons that cause sec-
 314 ondary ionisation in tube volume. The impact do only those electrons which are emitted in the
 315 direction of the wire(see example on fig.19a).

316 The number of events out of TR-ralation because of δ -electrons is quite small. Especially
 317 percentage of events where δ -electrons make effect on drift time is less than 1% of total number
 318 of events in GARFIELD simulations.

319 Tube wall is very thin but particle still can cause δ -electrons when crossing it. GEANT4
 320 studies show that such kind effect also presents in interaction of muon with tube volume, and
 321 percentage of events with δ -electron that affect drift time even less than 0.2%.

322 7.2 Finding of rt-relation

323 The rt-relation depict relation between drift time and track position. The idea is to find the
 324 best fit of give data to achieve higher resolution and avoid systematic errors.

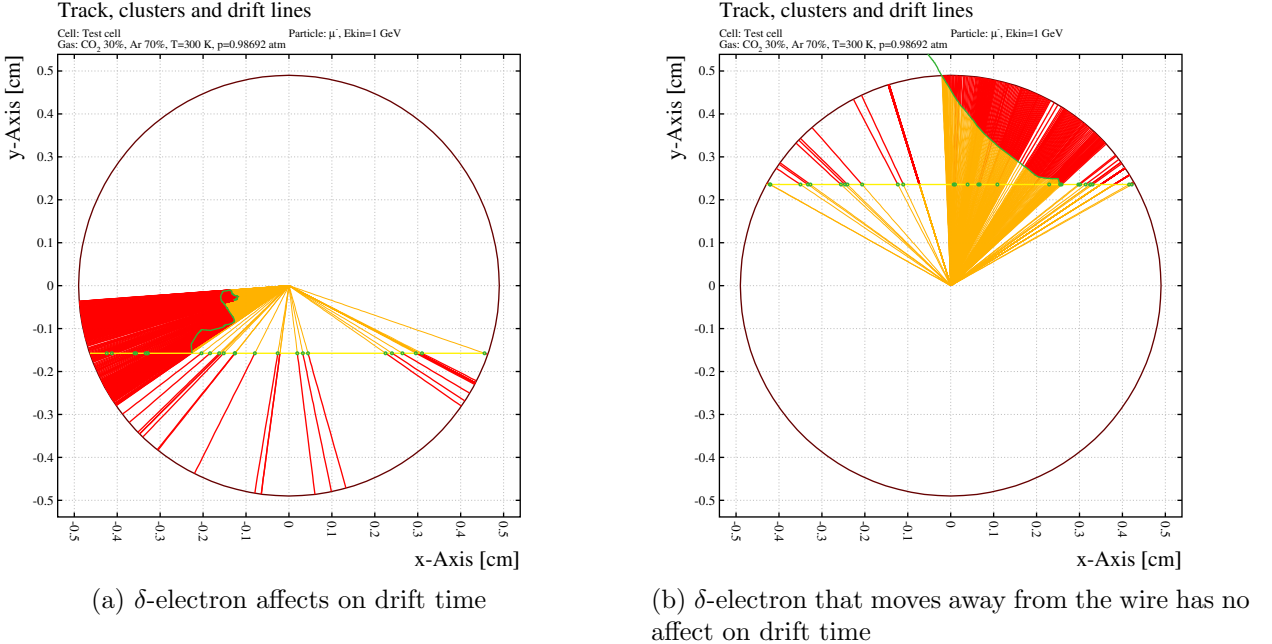


Figure 19: Garfield simulation with δ -electron presence. Red lines - ion trajectory, yellow - electrons. Trajectory of δ -electron marked by green curve line.

325 The problem that we have to minimize influence of noise while fit. One suppose that the
 326 noise have approximately homogeneous distribution of points that locates below the main line
 327 of distribution. Consequently we can filter it by fitting only points from regions with local point
 328 density higher than some threshold value. Another way is to make a binning our distribution
 329 along the track position and fit every 1-D histogram by Gaussian. The fit points of Gaussian
 330 mean values by fit function.

331 Nevertheless our data contain very small amount of "non-track" points.

332 TR-relation is asymmetry relatively to the $r = 0$ almost in all cases except wire in the center
 333 of the tube. Therefore we have to calibrate for every of branches. It means we need to find two
 334 track positions for every of drift time value and reject one of them in further data processing
 335 stages.

336 In previous section we found way to measure wire sag profile. So we can use this trick in
 337 present stage for separating data into "right" and "left" branch. Every of branches we will
 338 calibrate separately.

339 Lets suppose we can fit every of tr-diagram by pair of analytic fit function (8):

$$t(r_{track}) = e^{a_0 + a_1 r_{track}} \quad (8)$$

340 If the figure ?? you can see tr-relation. Fitting is not perfect because of using simple fit
 341 function template (8). But we will use reverse to the (8) relation, because we have to find r_{track}
 342 from known t_{drift} . We can do it be because the aim of this studies is not a precision calibration
 343 but global evaluation affect of wire sagging into total result.

344 As you can see in the figure ?? red fit line does not cover whole drift time spectre. So events
 345 with drift time less than covered range (less than $\sim 20\text{ns}$) counts as track through the wire:

$$r_{track}(t_{drift} < t_{min}) = r_{wire \ pos} \quad (9)$$

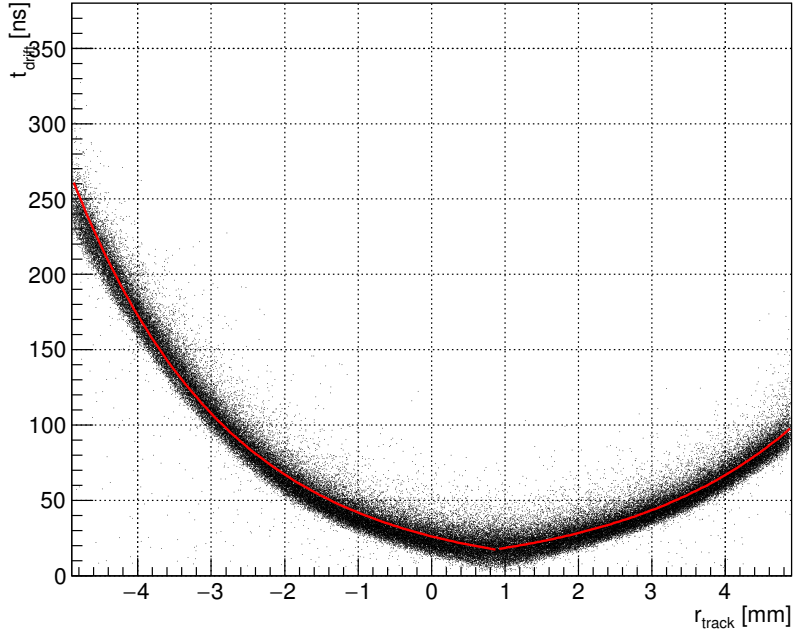


Figure 20: TR-relation fitting for 0.9mm wire offset value

346 where $t_{min} = \min(t_{drift}(r_{track}))$, $r_{track} = \overline{(-r_{tube}, r_{tube})}$. Respectively tracks with drift time
 347 higher than maximum of fit function range artificially counts as tracks with near tangents to
 348 the tube position $r_{track} = \pm r_{tube}$ (because efficiency decreases near the tube wall down to 20%).

349 7.3 Track reconstruction precision

350 Obviously precision is head factor when during we decide design of detector.

351 The STRAW tube tracker should be as light as possible to avoid multiple scattering on
 352 structural components of detector. But design should be changed within reason if precision
 353 suffers from this⁷.

354 How precision of track reconstruction depends on wire position(wire displacement)?

355 As you can see on figure ?? there are no significant difference of track reconstruction preci-
 356 sion between two mode of wire location despite of the increasing drift time for displaced wire
 357 position(with almost factor of two). The highest resolution($\sim 0.1mm$) near the tube wall and
 358 worst value $\sim 0.6mm$ is near the wire because the clustering effect. Higher gas pressure should
 359 resolve this problem.

⁷Especially design with no sagging works well for experiment NA62 []. But they have more than 2 times shorter straw when tube have insert in the middle of the tube. So sagging becomes negligible in this case.

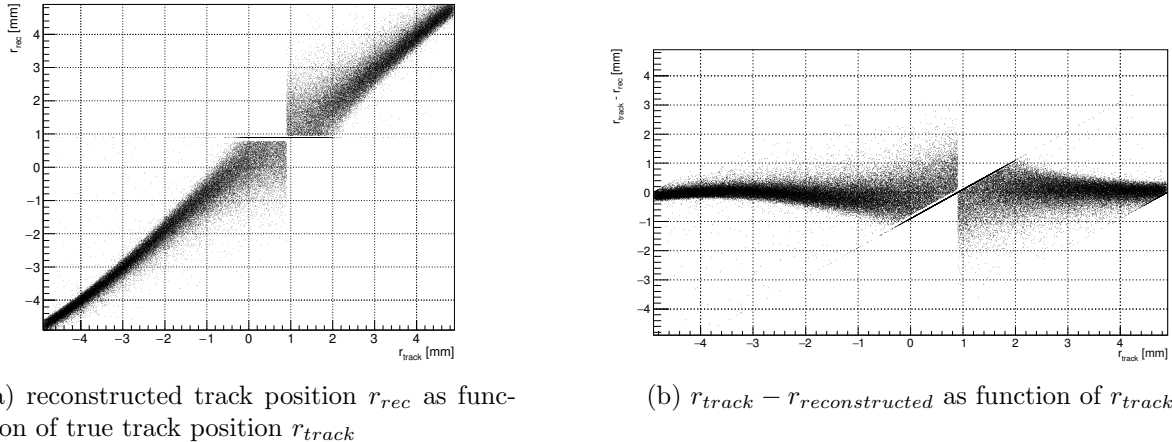


Figure 21: Distributions of matching of track position to their reconstructed value.

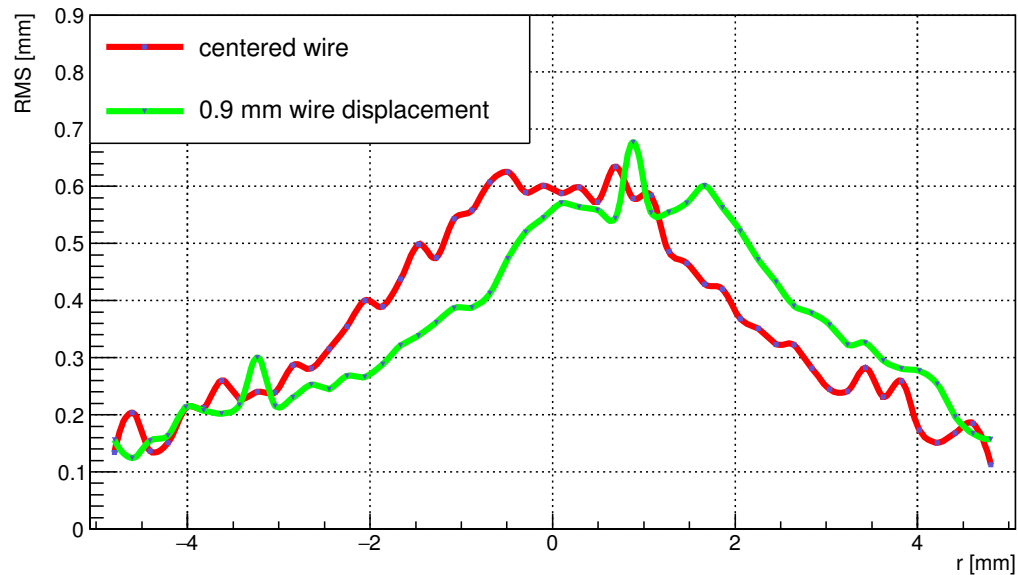


Figure 22: Comparison of track reconstruction precision for two wire position. Value of precision at every point means RMS of data sample near corresponding track position r . Red line corresponds to the centered wire position, green line – to the 0.9mm sagged wire position.

360 8 Measurements

361 We made measurements of some important drift tube parameters. We had tube of $\sim 50\text{cm}$
 362 length. But despite of short tube length we made there the length of the tube is not important.

363 The tube was manufactured in Dubna(Russian Federation) and was placed into the appropriate
 364 mechanics which include tube fixing, channels for supply of gas mixture, connector for
 365 grounding to the tube walls and connector for High Voltage (HV) supply.

366 The whole system is not compact, therefore we could not avoid the parasitic capacities. Now
 367 we will not go into details about it, as we have nothing to compare with because the system is
 368 non-separable.

369 The scheme of gas supply, circulation and control in the tube is shown in the Fig.23.

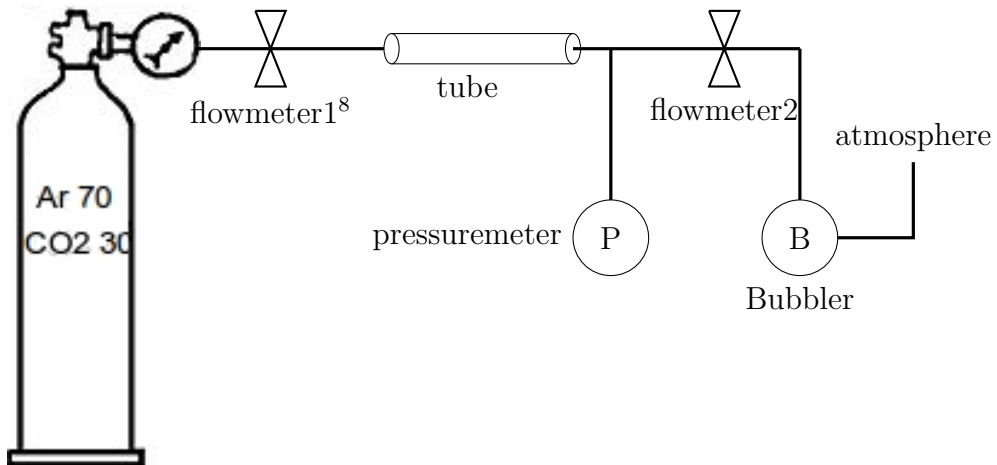


Figure 23: Gas circulation scheme and circuit of connection of flow control through the drift tube

370 The electric scheme of the drift tube connection is shown in the Fig.24.

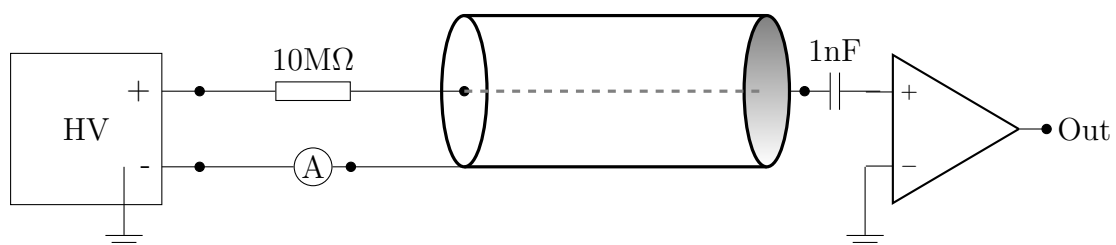


Figure 24: The electric scheme of the drift tube connection

371 As it is seen above, the scheme is very simple.

372 For our research we used a source Fe^{55} witch is suitable for a drift tube calibration. In our
 373 case Fe^{55} serves as a photon source with almost monochromatic spectra with energy 5.9 keV.

374 The most important parameter witch we have to measure a Gain G (3).

375 The idea is to measure a charge that goes thought the tube electric circuit per unit of time
 376 and then find a Gain. We assume that a current I_0 though the ampere meter(see fig. 24) is
 377 constant when the radioactive source is absent. The current is non-zero when the tube detects

378 background particles(for example atmospheric muon flux) or when a leakage current is present.
 379 Therefore, with the presence of a source Fe^{55} all surplus of the current $\Delta I = I - I_0$ in the drift
 380 tube circuit occurs because of gamma ray detection.

381 On the other hand, we can write ΔI in terms of initial amount of electrons and Gain in
 382 the following form :

$$\Delta I = GN_0e, \quad (10)$$

383 where G – Gain; N_0 - number of initial electron-ion pairs per second; e - charge of electron
 384 in C.

385 On the other hand we can express N_0 as:

$$N_0 = R \cdot \langle n \rangle = R \cdot \sum_n np(n) \approx R \int_0^{\infty} np(n)dn; \quad (11)$$

386 where $p(n)$ is a probability that the photon with energy 5.9 keV after interaction with
 387 argon atom will create n electron-ion pairs; R is a rate [Hz], as we need to find the amount of
 388 electron-ion pairs per one second.

389 The calculation of the distribution $p(n)$ in GARFIELD is shown in Fig.???. In the figure
 390 we can see the two peaks: the main photopeak and the smaller escape peak. The escape peak
 391 for argon is known to be 3.2 keV less than the primary peak. An escape peak is formed by
 392 a number of photon interactions in the gas resulting in one primary ionization electron and a
 393 re-emitted X-ray with a long mean free path.

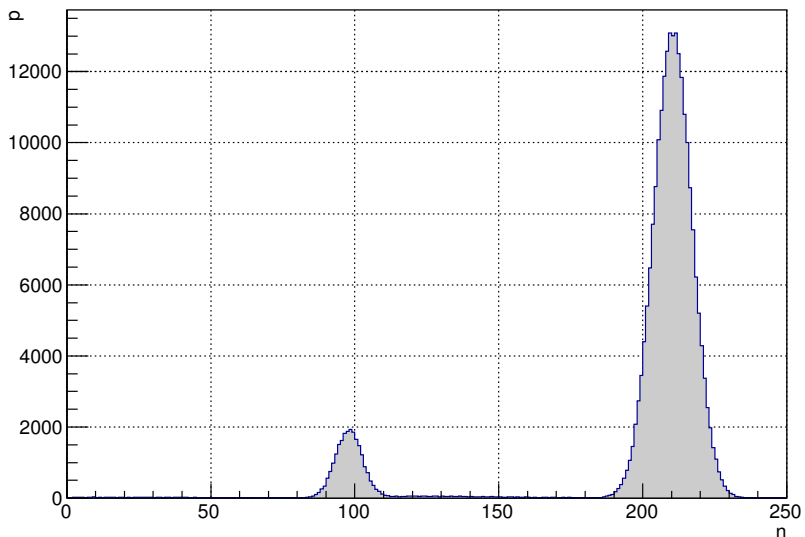


Figure 25: $p(n)$ distribution

394 The realisation of a measurement is very simple. On the output of amplifier(see Fig.24)
 395 the signal goes to the discriminator with trigger threshold on the level enough for a signal
 396 detection and big enough for noise neglecting. The signal from discriminator goes into counter
 397 in rectangle form. The counter triggering for the rising edge. This scheme has a small dead

398 time $0.5\mu s$, therefore for the signal frequency of $R \sim 5000 \frac{\text{events}}{\text{second}} \approx 200 \frac{\mu s}{\text{event}}$ the amount of non
 399 counted signal is negligibly small.

400 For the first gain estimation we assume about avalanche superposition and linear amplitude
 401 dependence of final signal on the amount of initial electrons(later we will show that this is not
 402 true).

403 From the distribution in Fig.25 we can find $\langle n \rangle = 197.87$ for average amount of primary
 404 electron because of photon(5.9keV) interaction with atoms of a gas $Ar70\% + CO_230\%$.

405 The results of measurements are shown in the table 3. The Gain curves G(V) for several
 406 pressure values are shown in the Fig.26.

Gain(no cor)	P[bar] (U[V])	HV [V]	Thr [mV]	I [nA]	RMS [nA]	Rate [Hz]
11138	1.0(0.857)	1600		1.7700	0.0919	=
18196	1.0(0.857)	1650		2.8915	0.1598	=
29255	1.0(0.857)	1700	32	4.6490	0.2328	4965.9
47012	1.0(0.858)	1750		7.4707	0.4380	=
73159	1.0(0.857)	1800		11.6257	0.5630	=
9885	1.106(0.906)	1650		1.6921	0.1099	=
15747	1.106(0.905)	1700		2.6955	0.13381	=
25275	1.106(0.905)	1750	32	4.3263	0.1975	5349.0
39887	1.106(0.906)	1800		6.8274	0.2841	=
61359	1.106(0.906)	1850		10.5028	0.4567	=
9260	1.205(0.951)	1700		1.6921	0.1053	
14536	1.205(0.951)	1750		2.6562	0.1274	
22991	1.205(0.951)	1800	32	4.2012	0.1900	5710
35777	1.205(0.951)	1850		6.5376	0.2880	
54684	1.205(0.951)	1900		9.9924	0.5284	
5444	1.309 (0.998)	1700		1.03	0.06	
8351	1.309 (0.998)	1750		1.58	0.14	
13267	1.309 (0.998)	1800		2.51	0.12	
20615	1.309 (0.998)	1850	32	3.90	0.15	5987
31716	1.309 (0.998)	1900		6.00	0.29	
48102	1.309 (0.998)	1950		9.10	0.38	
69987	1.309 (0.998)	2000		13.24	0.50	
100751	1.309 (0.998)	2050		19.06	0.78	

Table 3: Gain measurements

407 8.1 Experimental spectra from the source Fe55

408 Fe^{55} is a source of gamma-rays with energy of 5.9 keV. Each signal at the output of amplifier
 409 differs by amplitude in dependence of initial electron number. Therefore, according to the cal-

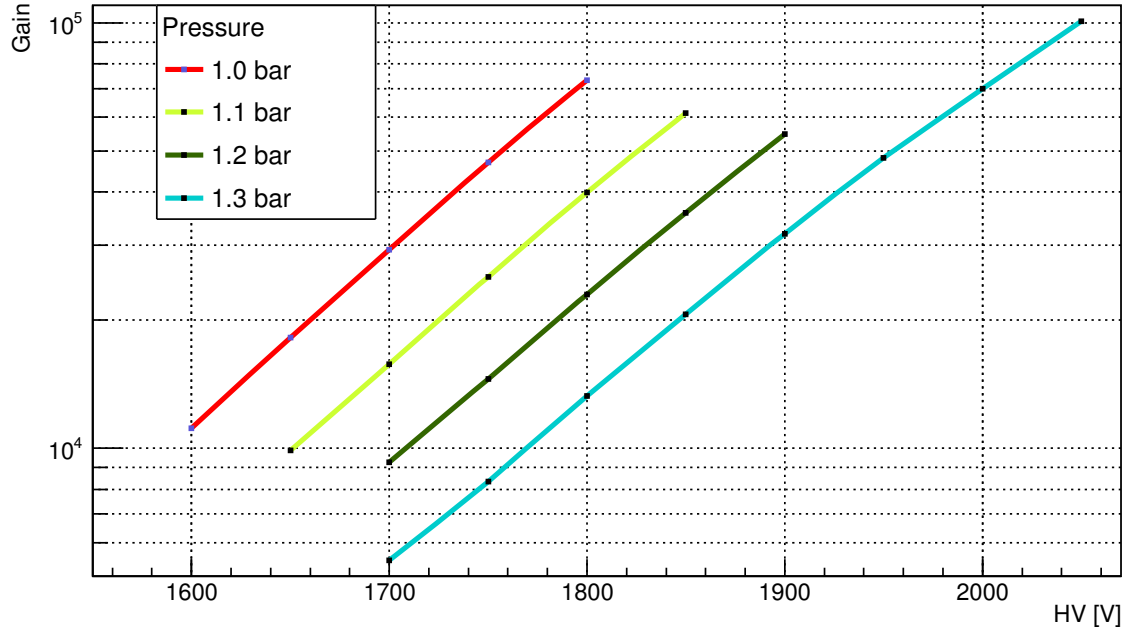


Figure 26: Gain experimental curves for several values of gas pressure in the drift tube.

410 culated in GARFIELD spectra $p(n)$ (see Fig.25), it is expected to see two peaks in experimental
 411 spectra.

412 For spectra measurements we first have to get a match between a certain signal and the
 413 amplitude on the output of the drift tube. In our case such a quantity is an integral from a
 414 signal on during the time of a signal.

415 The amplified signal from the output of the amplifier is sent in parallel through the linear
 416 splitter to the discriminator and delay system. With the signal from discriminator the sampling
 417 signal and busy signal is formed. During the busy signal the analysing system does not accept
 418 the signal from the drift tube (this is a dead time for this detector system). The delayed
 419 signal from the amplifier integrates during the sampling signal and then digitalizes with 10-bit
 420 ADC. After digitalizing the signal is sent through the optical channel to PC, where the data is
 421 recorded into separate ROOT-file.

422 The stages *sampling + storing* are time-consuming and a dead time in this case is bigger than
 423 an average time interval between events in the tube (with current detector system) therefore is
 424 a big probability to miss detecting an event.

425 The sampling stage is built in such a way to calibrate for pedestal shelf voltage from the
 426 integrator. On the final histogram it will look as a small peak. We will calibrate exactly with
 427 regard to it. The second control point is a gamma-ray 5.9 keV photo peak from the source
 428 Fe^{55} .

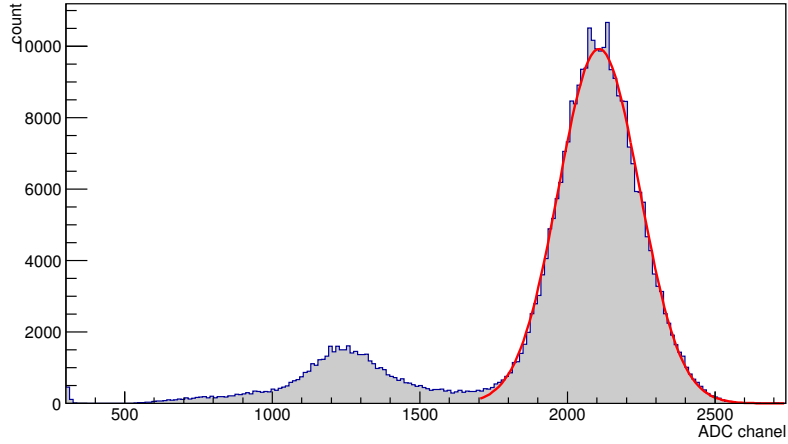


Figure 27: Experimental spectra from Fe^{55} .

point of reference	channel	electrons per cluster(simulations)
zero pedestal (<i>gauss</i> $\mu \pm \Delta\mu$)	301.1 ± 0.3	0
5.9 keV	2107.4 ± 0.3	210.42 ± 0.01
escape peak	1253.3 ± 0.9	97.99 ± 0.03

Table 4: Coordinates of peaks from Fig.27 and Fig.25

429 8.2 Space charge effect

430 Photons from Fe^{55} of energy 5.9 keV create ~ 200 electron-ion pairs as a result of photoeffect
 431 with $Ar70\% + CO_230\%$ gas mixture. As we have a strong electric field between anode and
 432 cathode such electron cloud starts to drift toward a wire. The external field distorts as any
 433 space charge creates its own e/m field. As a result, partial avalanches per initial electron of
 434 a cloud creates an avalanche of size smaller than from a single-electron cloud(as in case muon
 435 ionisation).

436 Such an effect indeed was observed. If we suppose a linear dependence of output signal
 437 amplitude from number of initial electrons a relative position for experimental peak should be
 438 located at(calibration relatively to the photopeak):

$$channel_{escapePeak} = \frac{2107.4 - 301.1}{210.42} 98 + 301.1 = 1142.3 \neq 1253.3, \quad (12)$$

439 **9 Appendix**

440 **9.1 pressure meter**

441 For the pressure measurement inside of drift tube we used pressure transmitters from
442 SensorTechnics®. The devise is marked by ID:CTE9005AQ4, so we used appropriate datasheet
443 from the manufacturer [5].

444 According to datasheet and marking, this pressure transmitter is designed for pressure mea-
445 surements in the interval $0 \dots 5 \text{ bar}$. But on the transmitter is marked an interval $0 \dots 3,5 \text{ bar}$.
446 So to be able to use this devise, we additionally calibrated it.

447 For this purpose we used two control points: the output current value for atmospheric
448 pressure at that point (727 mmHg) and a current for a vacuum. To get a vacuum we used a
449 pump which decreases a pressure to the value $< 0.001 \text{ bar}$ which we consider as a vacuum.

Table 5: Control points for calibration of pressure transmitter.

pressure [bar]	voltage[V]
0.001	0.405
1	0.858

450 Therefore the voltage dependence taken on a resistor 100Ω depends on a pressure as:

$$V = 4.05 + 0.453 \cdot P[\text{bar}] \quad (13)$$

$$P[\text{bar}] = -0.894 + 2.2075 \cdot V \quad (14)$$

451 **References**

- 452 [1] <http://garfield.web.cern.ch/garfield>
- 453 [2] thesis Kozlinskiy.pdf
- 454 [3] Technical Proposal from 8 april 2015: arXiv:1504.04956v1
- 455 [4] F. Hahn, F. Ambrosino, A. Ceccucci, H. Danielsson, N. Doble, F. Fantechi, A. Kluge, C.
456 Lazzeroni, M. Lenti, G. Ruggiero, M. Sozzi, P. Valente, and R. Wanke. NA62: Technical
457 Design Document. Technical Report NA62-10-07, CERN, Geneva
- 458 [5] DataSheet for Pressure transmitters for corrosive liquids and gases CTE/CTU9000 series.
459 http://www.first-sensor.com/cms/upload/datasheets/DS_Standard-CTE-CTU9000_E_11509.pdf
- 460 [6] W. Bonivento, A. Boyarsky, H. Dijkstra, U. Egede, M. Ferro-Luzzi, B. Goddard, A. Golubtin,
461 D. Gorbunov, R. Jacobsson, J. Panman, M. Patel, O. Ruchayskiy, T. Ruf, N.
462 Serra, M. Shaposhnikov, and D. Treille. Proposal to Search for Heavy Neutral Leptons at
463 the SPS. Technical Report CERN-SPSC-2013-024. SPSC-EOI-010, CERN, Geneva (Oct,
464 2013).
- 465